Investigation of Gas–Solid Bubbling Fluidized Beds Using ECT with a Modified Tikhonov Regularization Technique

Qiang Guo [ID]

Dalian National Laboratory for Clean Energy and National Engineering Laboratory for MTO, Dalian Institute of Chemical Physics, Chinese Academy of Sciences, Dalian 116023, China

University of Chinese Academy of Sciences, Beijing 100049, China

Shuanghe Meng, Dehu Wang, Yinfeng Zhao, and Mao Ye

Dalian National Laboratory for Clean Energy and National Engineering Laboratory for MTO, Dalian Institute of Chemical Physics, Chinese Academy of Sciences, Dalian 116023, China

Wuqiang Yang

School of Electrical and Electronic Engineering, The University of Manchester, Manchester M13 9PL, U.K.

Zhongmin Liu

Dalian National Laboratory for Clean Energy and National Engineering Laboratory for MTO, Dalian Institute of Chemical Physics, Chinese Academy of Sciences, Dalian 116023, China

Electrical capacitance tomography (ECT) provides a non-intrusive means to visualize cross-sectional material distribution of gas–solid bubbling fluidized beds. Successful application of ECT strongly depends on the image reconstruction algorithm used. For on-line measurements of bubbling fluidized beds, employing an algorithm that can produce high-quality images without extensive computation is necessary. Using the conventional Tikhonov regularization algorithm, image quality in the central area is basically satisfied but suffers from artifacts in the near-wall region. To solve this problem, a similar division operation learned from linear back projection was introduced to modify the conventional Tikhonov algorithm. Both numerical simulations and experiments were performed to evaluate the modified technique. The results indicate that the artifacts can be effectively removed and the reconstructed image quality is similar to Landweber method with dozens of iterations. Furthermore, the modified Tikhonov technique shows high accuracy when obtaining important hydrodynamic parameters in gas–solid bubbling fluidized beds. © 2017 American Institute of Chemical Engineers AIChE J, 64: 29–41, 2018
Keywords: gas–solid bubbling fluidized bed, electrical capacitance tomography, image reconstruction algorithm, Tikhonov regularization, hydrodynamic parameter

Introduction

Gas–solid bubbling fluidized bed reactors are used in many industrial processes, such as coal gasification, power generation, granulation, and polymerization. To measure hydrodynamic characteristics of gas–solid bubbling fluidized beds, numerous intrusive and non-intrusive experimental techniques have been developed.[1–6] The intrusive methods like optical probe,[2,5] capacitance probe,[1,2,5] and pressure measurement[2,4] are easy to implement but only capable of providing local information concerning the fluid flow. While the non-intrusive techniques such as tomography[3] can be used to visualize the

entire flow field without causing any disturbance to the flow. Compared to other industrial process tomography techniques, electrical capacitance tomography (ECT) shows advantages in terms of fast imaging speed, no radiation, robustness, and low cost.[7] Moreover, considering the non-conductive nature of materials in gas–solid bubbling fluidized beds, ECT is a suitable measuring technique for hydrodynamic investigation of these reactors.[6,8–13]

In ECT, the sensing electronics measure variations in capacitance between pairs of electrodes, which are placed around the periphery of a pipe or vessel under investigation. These measurements are then used to reconstruct cross-sectional permittivity distribution as a presentation of material distribution inside the sensing area via a sensitivity theory-based image reconstruction algorithm.[14–16] However, two major difficulties are associated with the reconstruction process.[15] First, the number of measured independent capacitance data is far less than the number of unknown image pixels, and therefore the

---

problem is severely under-determined. Second, due to the ill-posed and ill-conditioned property of the reconstruction process, the reconstructed results are sensitive to raw capacitance measurement noise. To address these problems, different reconstruction techniques, including single-step and iterative algorithms, have been proposed and have been reviewed by Yang and Peng[15] and Cui et al.[17] Among all the proposed algorithms, linear back projection (LBP), Tikhonov regularization, and Landweber iteration are three most popular methods,[18–20] in which the former two are single-step while the latter is iterative.

As an example, Supporting Information Figure S1 shows some typical results reconstructed by these three algorithms. As can be seen, the LBP method can only give qualitative images in all cases. The results of the Tikhonov regularization are basically satisfied in the central area, even with multiple objects like four rods and four bubbles. However, the biggest problem associated with the Tikhonov regularization is that some unphysical artifacts appear in the near-wall region,[15,21,22] especially in the case of low-permittivity materials presenting in a high-permittivity background, which is exactly the case in a gas–solid bubbling fluidized bed, where discrete bubbles are dispersed in a continuous emulsion phase with a shell of solid particles in which solid concentration increases continuously.[23] When the Landweber iteration is used, the best images can be obtained in almost all cases[15]; however, it can only be applied as an off-line reconstruction method due to its slow reconstruction speed.

Allowing for the dynamics of gas–solid bubbling fluidized bed reactors, a non-iterative algorithm has to be used for on-line measurements. Owing to its simplicity and fast speed,[6,12,24] the LBP method is always the first choice. However, image quality reconstructed by the LBP is relatively poor. For the Tikhonov regularization, even though it is a well-established technique to solve ill-posed problems[25] and has been extensively used in ECT image reconstruction,[19,21,26] the severe problem of artifacts restricts its practical application.

In general, a generic sensitivity matrix calculated based on a vacuum permittivity distribution is used for both single-step and iterative algorithms,[15,22,27] while it will change with different permittivity distributions because of the "soft-field" nature of ECT.[7,15] Using a sensitivity matrix updated by the actual permittivity distribution, Xue et al.[22] found that image quality reconstructed using the Tikhonov regularization could be improved and that the artifacts in the reconstructed images could be reduced. However, updating the sensitivity matrix is not practical for on-line image reconstruction. The reasons are twofold: (1) the true distribution is unknown in real applications and (2) updating the sensitivity matrix would take much more time.[24,25] Therefore, the method of Xue et al.[22] is not feasible for on-line ECT measurements.

By relating sensitivity distribution in the generic sensitivity matrix to images reconstructed by the conventional Tikhonov regularization method, we found that the non-uniform sensitivity distribution, which results from the "soft-field" nature of ECT,[14] is responsible for the artifacts appearing in the near-wall region. However, previous efforts that have been devoted to improving the conventional Tikhonov regularization method primarily focused on the modification of filter function,[28,29] optimized objective function,[19] and mathematical model to obtain the optimal value of regularization parameter.[30,31] To date, little work has been attempted to reduce the artifacts by considering the "soft-field" nature of ECT.

Referring back to Supporting Information Figure S1, it is important to highlight that, even though images obtained using the LBP method show poor quality in the central area, there are no artifacts in the near-wall region. Peng et al.[32] have also confirmed that the LBP can provide good image quality for annular and stratified distributions. Inspired by this finding, in this work we propose a modified Tikhonov regularization method that scales each pixel gray in the imaging area using a division operation, which was originally used in the LBP method, to eliminate the artifacts and hence enhance the image quality. To evaluate the applicability of the proposed algorithm to ECT measurements of gas–solid bubbling fluidized beds, numerical simulations, in which computational fluid dynamics (CFD) simulation results were used as permittivity distribution inputs, as well as bubbling fluidized bed experiments, were performed. In this way, the accuracy of the proposed algorithm when obtaining some key hydrodynamic parameters in gas–solid bubbling fluidized beds, such as overall solid concentration, bubble size, and radial profile of solid concentration, was verified.

The results show that not only the image quality but also the hydrodynamic parameters obtained by the modified Tikhonov method are comparable to those obtained by the Landweber iteration algorithm but with a significantly reduced computational time. Therefore, it is expected that the modified Tikhonov regularization algorithm can potentially be used as an efficient on-line image reconstruction method for ECT measurements of gas–solid bubbling fluidized beds. In fact, the proposed algorithm can also be applied to ECT measurements of bubble columns,[33,34] where low-permittivity gas bubbles are surrounded by a high-permittivity liquid phase.

ECT Model and Image Reconstruction Algorithms
ECT model

Peng et al.[32] concluded that 12-electrode ECT sensors can provide the best images in most cases; therefore a circular 12-electrode ECT sensor with an electrode covering ratio of 0.9, as shown in Supporting Information Figure S2, was modeled. The electrode covering ratio refers to the ratio of the arc length of all electrodes to the circumference of the investigated bed. It has been confirmed by Ye et al.[35] that an electrode covering ratio of 0.9 for a 12-electrode ECT sensor can achieve good image quality.

There are two major computational problems involved in the ECT model: the forward problem and the inverse problem.

The ECT forward problem is to calculate inter-electrode capacitance from a predefined permittivity distribution and is expressed as

$$C_M = -\varepsilon_0 \frac{1}{V} \int\int_\Gamma \varepsilon_r(x,y) \nabla \varphi(x,y) d\Gamma \tag{1}$$

where ε_0 is the permittivity of vacuum, V is the potential difference between the calculated electrode pair, $\varepsilon_r(x,y)$ and $\varphi(x,y)$ are the relative permittivity and potential distributions in the sensing domain, respectively, and Γ is the electrode surface. The number of independent capacitance measurements for a 12-electrode ECT sensor is 66.

Because Eq. 1 is too complicated, a simplified linear equation in a normalized form[15,17,27] is always used:

$$\lambda = Sg \tag{2}$$

where g is the normalized permittivity and λ is the normalized capacitance defined as

$$\lambda = \frac{C_M - C_L}{C_H - C_L} \tag{3}$$

where C_M is the measured capacitance for an arbitrary permittivity distribution and C_H and C_L are the capacitances when

the sensor is full of high- and low-permittivity materials, respectively.

The parameter S in Eq. 2 represents the normalized sensitivity matrix, which refers to the change in the normalized capacitance of each electrode pair in response to a perturbation of the normalized permittivity distribution. The construction of the sensitivity matrix requires discretization for implementation. Usually, the sensing area is subdivided into $n \times n$ square pixels, which results in N effective pixels in the circular imaging area. The choice of n (or N) is a trade-off between image resolution and the under-determined nature of the inverse problem of ECT.[36] Typically, N is of the order of magnitude of 1000. In particular, for a 12-electrode ECT sensor, a discretization with 64×64 pixels, which generates 3228 effective pixels in an ECT image, is normally used.[13,37]

Equation 4 is commonly employed to calculate the sensitivity matrix[22,27]:

$$S_{ij}^*(x,y) = -\iint_{p(x,y)} \frac{\nabla \varphi_i(x,y)}{V_i} \cdot \frac{\nabla \varphi_j(x,y)}{V_j} dxdy \qquad (4)$$

where S_{ij}^* defines the sensitivity between the ith and jth electrodes at the location of the pixel $p(x,y)$ and $\varphi_i(x,y)$ and $\varphi_j(x,y)$ are the potential distributions inside the sensing domain when the ith and jth electrodes are excited by applying voltages of V_i and V_j, respectively.

Thereafter, S^* is normalized as

$$S_{mn} = \frac{S_{mn}^*}{\sum_{n=1}^N S_{mn}^*} \qquad (5)$$

where S_{mn} and S_{mn}^* are the entries in the mth row and nth column of S and S^*, respectively.

Note that, while S will change with permittivity distribution, a generic S calculated based on a vacuum permittivity distribution[22,27] is commonly used for image reconstruction.

Image reconstruction algorithms

For the ECT inverse problem, the measured capacitance is transformed into a spatial permittivity distribution using a specific image reconstruction algorithm. In this section, three commonly used algorithms, i.e., LBP, conventional Tikhonov regularization, and projected Landweber iteration, are presented, followed by the modified Tikhonov regularization algorithm proposed in this article.

Linear Back Projection. LBP was the first algorithm developed for ECT.[14] The main principle of the LBP method is to replace the inverse of S, which is non-existent, with the transpose of S, as expressed by

$$\hat{g} = \frac{S^T \lambda}{S^T u_\lambda} \qquad (6)$$

where $\hat{g}$ is the reconstructed normalized permittivity and u_λ is a vector of ones with the same dimension as λ. The division operation in the LBP method is manipulated in a one-to-one mode.

Conventional Tikhonov Regularization. The formula of the conventional Tikhonov regularization algorithm is

$$\hat{g} = (S^T S + \mu I)^{-1} S^T \lambda \qquad (7)$$

where μ is the regularization parameter, which is a small positive number, and I is an $N \times N$ identity matrix with ones on the main diagonal and zeros elsewhere.
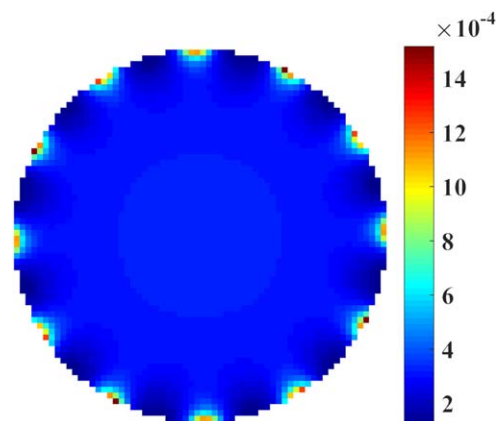

Figure 1. The spatial distribution of the normalized sensitivity averaged over all electrode pairs of the simulated ECT sensor.

The color scale represents the normalized sensitivity. [Color figure can be viewed at wileyonlinelibrary.com]

As is well known, it is crucial to choose a suitable μ to obtain a reliable estimation of the solution. However, in theory, determining μ is very difficult.[30,31] Therefore, this is usually done by trial and error.[15]

Projected Landweber Iteration. To improve the image quality, Landweber iteration with a projection was introduced to ECT[38] and is expressed as

$$\hat{g}_k = P\left(\hat{g}_{k-1} + \alpha_k S^T e_{k-1}\right) \qquad (8)$$

$$P[f(x)] = \begin{cases} 0 & \text{if } f(x) < 0 \\ f(x) & \text{if } 0 \le f(x) \le 1 \\ 1 & \text{if } f(x) > 1 \end{cases} \qquad (9)$$

where e_{k-1} is the deviation between the measured capacitance and the capacitance calculated from the $(k-1)$th reconstructed permittivity distribution, which is defined as

$$e_{k-1} = \lambda - S\hat{g}_{k-1} \qquad (10)$$

The initial estimation $\hat{g}_0$ in Eq. 8 is calculated by the LBP method as formulated in Eq. 6. A drawback to the Landweber iteration is its semi-convergence characteristic.[19] To improve the convergence speed, Liu et al.[39] suggested an optimal step length α_k during the iteration:

$$\alpha_k = \frac{\|S^T e_{k-1}\|}{\|SS^T e_{k-1}\|} \qquad (11)$$

Because the Landweber iteration algorithm has been confirmed to be capable of producing the best images in most cases[15] and is the most popular of iterative algorithms,[15,32,35,40] it is used as a reference to assess the new proposed algorithm.

Modified Tikhonov Regularization. Figure 1 shows the simulated ECT sensor's average sensitivity distribution, i.e., the spatial distribution of the normalized sensitivity averaged over all electrode pairs. It can be seen that, in the central area the sensitivity distribution is uniform, while in the near-wall region, a non-uniform distribution is clearly identified. More specifically, the gaps between two adjacent electrodes have the highest sensitivity, while the areas close to the electrodes have the lowest sensitivity. Considering this feature together with images reconstructed by the conventional Tikhonov regularization method as shown in Supporting
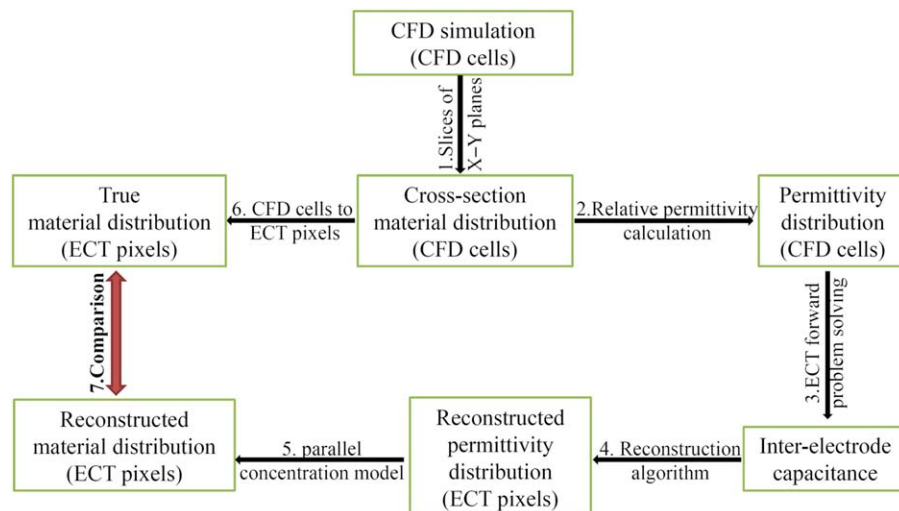
Figure 2. Procedure for the evaluation of image reconstruction algorithms using CFD simulation results as the input permittivity distributions.

[Color figure can be viewed at wileyonlinelibrary.com]

Information Figure S1 (and later in Figures 5 and 11 and Supporting Information Animation S1), it may be concluded that the main reason for the artifacts in the near-wall region is the non-uniform distribution of the sensitivity. Therefore, a scaling method similar to the division operation in the LBP method is proposed to modify the conventional Tikhonov regularization to

$$\hat{g} = \frac{(S^T S + \mu I)^{-1} S^T \lambda}{(S^T S + \mu I)^{-1} S^T u_\lambda} \quad (12)$$

Evaluation criteria

Three criteria, i.e., correlation coefficient (CC),[15,35,40] average absolute deviation (AAD),[16] and reconstruction speed,[15] are used to compare different image reconstruction algorithms in a quantitative manner. CC and AAD are defined, respectively, by Eqs. 13 and 14:

$$CC = \frac{\sum_{i=1}^{N} \left(\hat{g}_i - \bar{\hat{g}}\right)(g_i - \bar{g})}{\sqrt{\sum_{i=1}^{N} \left(\hat{g}_i - \bar{\hat{g}}\right)^2 \sum_{i=1}^{N} (g_i - \bar{g})^2}} \quad (13)$$

$$AAD = \frac{1}{N} \sum_{i=1}^{N} |\hat{\phi}_s - \phi_s| \quad (14)$$

where ϕ_s and $\hat{\phi}_s$ are the true and reconstructed solid concentration, respectively, and $\bar{g}$ and $\bar{\hat{g}}$ are the mean values of g and $\hat{g}$, respectively.

Correlation coefficient reflects the spatial similarity between the true and reconstructed images, and AAD represents the accuracy of an algorithm when reconstructing the solid concentration distribution. The best algorithm will give the maximum value of CC and the minimum value of AAD and will take the shortest reconstruction time.

Simulation and Experimental Setup

Numerical simulations

To evaluate the performance of different image reconstruction algorithms for ECT, it is common to carry out numerical simulations and/or experiments with stationary objects.[15,19–21,26,32] By this means, only some simple permittivity distributions such as those shown in Supporting Information Figure S1 can be tested. However, for gas–solid bubbling fluidized beds and other multiphase systems, true permittivity distributions are much more complex. In addition, the "soft-field" nature of ECT means that the electric field inside the imaging area can be distorted by the material present. Therefore, it is necessary to introduce the hydrodynamic characteristics of the investigated multiphase flow to the evaluation of an image reconstruction algorithm. Ye et al.[35,40] first reported such a framework based on a fluid-electrostatic field coupling method, in which the two-phase flow field and the electrostatic field are coupled by an additional electric force. However, the added electric force has no obvious effect on the hydrodynamic characteristics for the normally used excitation voltage, which is lower than 25 V.[40] Therefore, in this work, the coupling of the flow field and the electrostatic field is ignored and the CFD simulation results only serve as inputs for the image reconstruction in ECT, as suggested by Banaei et al.[16]

Figure 2 shows the procedure used in this work for the evaluation of image reconstruction algorithms using CFD simulation results as the permittivity distribution inputs. At first CFD simulation of a lab-scale bubbling fluidized bed of 14 cm in diameter and 1.5 m in height was performed with the kinetic theory of granular flow-based Eulerian granular model in Fluent 6.3. The 3-D geometry of the simulated fluidized bed is shown in Figure 3a, where gas enters the fluidized bed with a constant superficial gas velocity of 0.9 m/s from the bottom inlet and exits from an atmospheric pressure outlet located at the top. The 3-D mesh for the CFD simulation, as shown in an axial view in Figure 3b and in a cross-sectional view in Figure 3c, is composed of 1,199,900 hexahedra, which was generated based on O-grid technique with approximately $\Delta X \approx \Delta Y \approx$ 1.5 mm and $\Delta Z \approx 4$ mm. Note that the total number of CFD cells for any given cross-sectional plane is 3380. The wall boundary condition was defined following that by Sinclair and Jackson,[41] where a no-slip boundary condition was specified for the gas phase and a partial-slip boundary condition was used for the solid phase with a specularity coefficient of 0.6.

The initial bed height was set as 70 cm with an average solid concentration of 0.42. The physical properties of the gas phase and particles are listed in Supporting Information Table S1. More detailed CFD simulation settings are summarized in
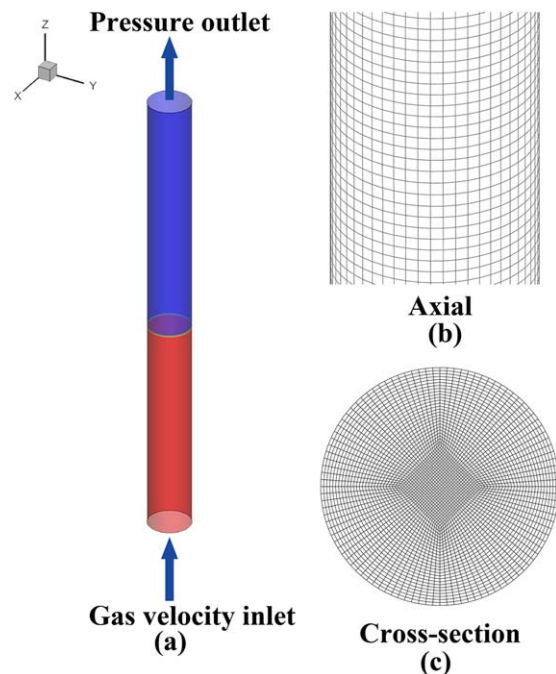
Figure 3. Geometry and mesh for CFD simulation of the bubbling fluidized bed.

[Color figure can be viewed at wileyonlinelibrary.com]

Supporting Information Table S2. To fully capture the bubble dynamics, the CFD simulation lasted 24 s and only the results in the last 18 s were extracted and used for the elevation of image reconstruction algorithms.

As a general rule, 3-D ECT problem is normally reduced to 2-D by neglecting axial hydrodynamics along the vertical height of the electrodes[7] and only reconstructing 2-D cross-section of the fluidized bed, representing the material distribution at the sensor's mid-position. To extract the cross-sectional solid concentration distribution from the CFD simulation results, apparently an average of the solid concentration distribution along the vertical height of the electrodes is more representative of reality. However, in this work we use the cross-sectional solid concentration distributions at several bed heights but do not average them over the vertical direction. This is because we use the simulated solid concentration distributions only as inputs to evaluate image reconstruction algorithms. In addition, all the following discussions using CFD simulation results as the input permittivity distributions are performed in 2-D. It should be emphasized that, however, the average of solid concentration distribution over the vertical height of the electrodes cannot be ignored if a direct comparison between the CFD simulation results and ECT experiments is desired.

As shown in Figure 2, upon completing the CFD simulation, the 2-D cross-sectional solid concentration distributions at bed heights of 20, 30, 40, 50, 60, 70, and 80 cm and at time points of 6, 9, 12, 15, 18, 21, and 24 s were extracted from the slices of the corresponding X–Y planes of the CFD simulation results (Step 1 in Figure 2). Then, to obtain the inter-electrode capacitance for a specified permittivity distribution, the material distribution in each CFD cell needs to be converted to the permittivity distribution (Step 2 in Figure 2), which was achieved via the calculation of the relative permittivity ε_r, as expressed by

$$\varepsilon_r = \varepsilon_s \phi_s + \varepsilon_g (1 - \phi_s) \tag{15}$$

where ε_g and ε_s are the relative permittivity of the gas and solid, respectively, as listed in Supporting Information Table S1. COMSOL Multiphysics and MATLAB were used to solve the ECT forward problem (Step 3 in Figure 2). The high permittivity used in the full calibration process was calculated from Eq. 15, where $\phi_s = \phi_{max} = 0.63$. Note that the electrostatic field simulation was performed using the CFD grid. The grid type used at each step is also indicated in Figure 2.

As previously mentioned, image reconstruction with ECT is sensitive to measurement noise. Previous studies[42,43] show that typical signal-to-noise ratio (SNR) for ECT systems is higher than 60 dB. Therefore, to include the effect of noise, 60 dB white Gaussian noise was added to the capacitance data prior to normalization, and the normalized capacitance was then calculated by

$$\lambda = \frac{(C_M + \delta_M) - (C_L + \delta_L)}{(C_H + \delta_H) - (C_L + \delta_L)} \tag{16}$$

where δ_M, δ_L, and δ_H are, respectively, the Gaussian distributed random noise added to C_M, C_L, and C_H.

Once the normalized capacitance was obtained, the permittivity distribution in each ECT pixel could be reconstructed by solving the inverse problem using an image reconstruction algorithm (Step 4 in Figure 2). Then, the reconstructed solid concentration $\hat{\phi}_s$ in each ECT pixel was obtained (Step 5 in Figure 2) by the parallel model,[16,44,45] in which the normalized permittivity equals the normalized solid concentration, and therefore

$$\hat{\phi}_s = \phi_{max} \hat{g} \tag{17}$$

Because any given cross-sectional plane of the CFD simulation consists of 3380 CFD cells, as shown in Figure 3c, which are different from those of the N square pixels in an ECT image, to make a comparison of the solid concentration between the true distributions from the CFD simulation results and the reconstructed distributions obtained by a specific image reconstruction algorithm, it is necessary to map the solid concentration at CFD grid to ECT pixels (Step 6 in Figure 2). The interpolation was achieved via the following procedure. First, each ECT pixel was divided into 10 × 10 ECT sub-pixels and, for each ECT sub-pixel, a partner CFD cell was defined based on the shortest distance between their center points. Then, each ECT sub-pixel was assigned a solid concentration that was the same as its partner CFD cell. Subsequently, the solid concentration for an ECT pixel was the average over the 10 × 10 ECT sub-pixels included in this pixel. Next, the obtained solid concentration in all the ECT pixels was used to construct an ECT square-pixel-style image. The converted distributions were later treated as the true distributions for comparison (Step 7 in Figure 2).

As an illustration, Supporting Information Figure S3a shows a typical cross-sectional solid concentration distribution obtained from the CFD simulation results. The corresponding ECT images interpolated from the CFD grid are shown in Supporting Information Figures S3b–S3d for image resolutions of 48 × 48 pixels, 64 × 64 pixels, and 80 × 80 pixels, respectively. Note that the numbers of effective pixels in the circular imaging area for Supporting Information Figures S3b–S3d are 1804, 3228, and 5024, respectively. It is clear from Supporting Information Figure S3 that overall the three image resolutions considered in current study can be
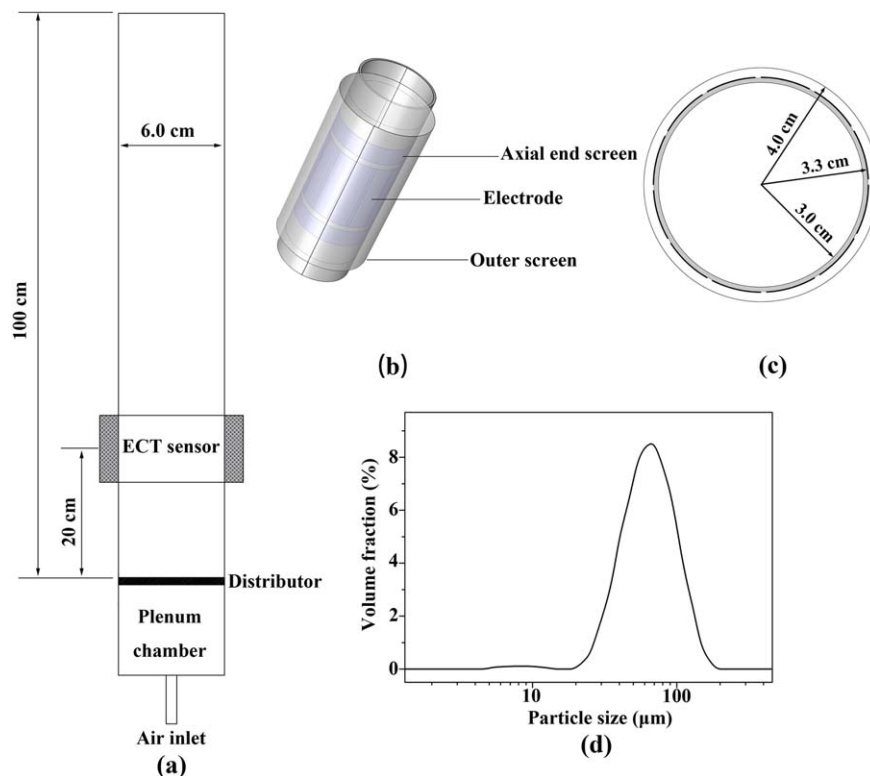
Figure 4. Experimental setup.

[Color figure can be viewed at wileyonlinelibrary.com]

satisfactorily used to reconstruct the original distributions. However, the images with higher resolutions, i.e., 64 × 64 and 80 × 80 pixels, can show more details on the gradual change of solid concentration between bubble and emulsion phases compared to that with a relatively low resolution of 48 × 48 pixels. Because the number of effective pixels in an ECT image given by the discretization with 64 × 64 pixels is 3228, which is very close to the number of CFD cells for any given cross-sectional plane, say 3380, the discretization with 64 × 64 pixels can give a similar resolution to the CFD simulation results, which makes the comparison between the original solid concentration distribution and the reconstructed ECT image more straightforward. In these regards, the discretization with 64 × 64 pixels was employed throughout this work. In fact, it was found that the tested pixel discretization only has a minor effect on the performance of different image reconstruction algorithms (see Supporting Information Figure S4); therefore, the choice of the discretization with 64 × 64 pixels will not influence the evaluation of image reconstruction algorithms.

Experimental setup

To validate the simulation results and further verify the feasibility, as well as the noise immunity, of the modified Tikhonov regularization algorithm, a cylindrical bubbling fluidized bed equipped with a 12-electrode ECT sensor was set up, as shown in Figure 4a. The fluidized bed was made of quartz glass and had a height of 1 m, an inner diameter of 6.0 cm, and an outer diameter of 6.6 cm. Airflow under ambient conditions was introduced to the fluidized bed through a porous polypropylene plate with a mean pore size of 10 μm. The fluidized particles were fluid catalytic cracking (FCC) catalysts with the Sauter mean diameter of 65 μm (the particle size distribution is shown

in Figure 4d) and particle density of 1370 kg/m³, which are typical Group A particles according to Geldart's classification.[46] Preliminary tests revealed that the minimum fluidization velocity and minimum bubbling velocity of the FCC particles were 2.75 and 9.95 mm/s, respectively.

Figure 4b shows the used 12-electrode ECT sensor whose cross-sectional dimensions are detailed in Figure 4c. The ECT electrodes, with a vertical height of 3 cm, were stuck onto the outside wall of the fluidized bed. The width of the electrodes was chosen in such a way that the covering ratio of the electrodes was the same as that used in simulations. The mid-position of the sensor was located 20 cm above the distributor. Hence the measurement region encompassed a height between 18.5 and 21.5 cm above the distributor, and thus each pixel in an ECT image represented an axial average over this measurement volume. An AC-based ECT system[18] was applied for capacitance measurement. The SNR of the used ECT system is approximately 73 dB, which is somehow higher than that was used in simulations. Before the measurement, air and packed bed of FCC catalyst particles with a static height of 33 cm were used to obtain C_L and C_H in Eq. 3, respectively, to calibrate the ECT system. To make the bed operate in bubbling regime, the superficial gas velocity was controlled between 1.17 and 12.8 cm/s with a step of 1.17 cm/s. For each velocity, a total of 10,000 sets of capacitance data were collected, which corresponds to a period of 100 s as the data acquisition rate of the ECT system is 100 frames per second.

Results and Discussions
Evaluation by simulations

To evaluate the performance of different image reconstruction algorithms using CFD simulation results as the inputs, 78
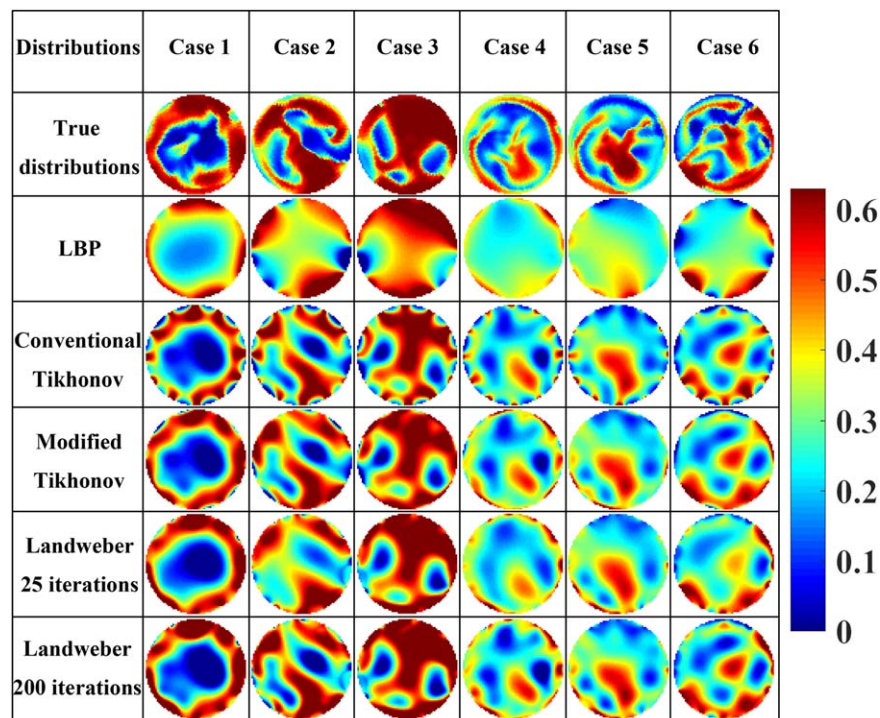
Figure 5. Cross-sectional solid concentration distributions reconstructed by different algorithms using CFD simulation results as the input permittivity distributions.

The color scale represents the solid concentration. [Color figure can be viewed at wileyonlinelibrary.com]

randomly selected true distributions were used as reference distributions for reconstruction. Animations of these 78 selected solid concentration distributions and the corresponding images reconstructed by different image reconstruction algorithms are displayed in Supporting Information Animation S1. These 78 distributions represent the appearances of a single bubble, two bubbles, and multiple bubbles located at different positions, which can reflect notable bubble dynamics in a gas–solid bubbling fluidized bed such as bubble growth, coalescence, and movement. All the following discussions are based on these selected distributions.

Determination of the Regularization Parameter. The quality of images reconstructed by the Tikhonov regularization algorithm strongly depends on the regularization parameter μ. It is generally accepted that a small value of μ can give a good approximation to the solution but a too small value of μ may lead to a singularity. Typical values of μ for the conventional Tikhonov algorithm range from 0.0001 to 0.1.[16,21,28] To find the optimal value of μ for both the conventional and modified Tikhonov regularization algorithms for the simulated sensor, a wide range of μ, from 1×10^{-9} to 100, was tested to explore the dependence of CC and AAD on μ. The results are shown in Supporting Information Figure S5. Note that a value of μ smaller than 1×10^{-9} can make the matrix $S^T S + \mu I$ close to singular. In accordance with the evaluation criteria, the most appropriate value of μ for the simulated ECT sensor is 0.0001 for both Tikhonov regularization methods.

From the comparison in Supporting Information Figure S5, it is clear that the modified Tikhonov method improves CC and AAD with all tested values of μ. In particular, a higher value of μ in the magnitude of 100, which is too large for the conventional Tikhonov regularization method, is still acceptable for the modified algorithm. We currently do not know the

reason for the wider range of μ in the modified Tikhonov regularization, which anyway deserves further research.

Image Quality Comparison. Figure 5 shows six typical cases that are included in Supporting Information Animation S1. By comparing the reconstructed solid concentration distributions to the reference images, it can be seen that the LBP method produces high-quality images near the wall, while details in the central region are all blurred due to the lower sensitivity there and eventually only simple distributions such as the single-bubble distribution in Case 1 can be reconstructed. Conversely, the conventional Tikhonov regularization can produce the solid concentration distribution with good quality except for the artifacts in the near-wall region. A careful check suggests that the artifacts are formed with high solid concentration displayed in the pixels between two adjacent electrodes, while low solid concentration in the pixels near the electrode surface, which is akin to the sensitivity distribution in the generic sensitivity matrix, as shown in Figure 1. After the modification made by the division operation in the conventional Tikhonov regularization algorithm, the artifacts disappear, as shown in the fifth row of Figure 5, and the image quality is improved for all tested cases. A further comparison between the modified Tikhonov regularization and the Landweber iteration indicates that nearly all images reconstructed by the modified Tikhonov technique are similar to those reconstructed by the Landweber algorithm with 25 iterations (see Supporting Information Animation S1). In the presence of complex multi-bubble distributions, such as in Cases 2, 4, and 6 shown in Figure 5, the modified Tikhonov technique can even produce images as good as those produced by the Landweber algorithm with 200 iterations.

In Figure 6, CC and AAD obtained by different image reconstruction algorithms are compared, where CoTi and MoTi represent the conventional and modified Tikhonov
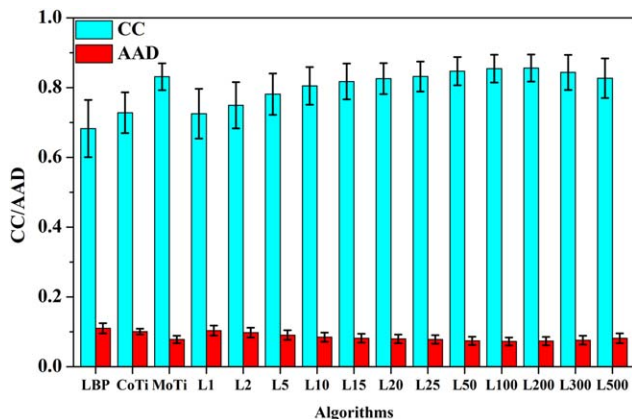
Figure 6. Quantitative comparison of different image reconstruction algorithms.

The error bars represent the standard deviation over the 78 tested distributions. [Color figure can be viewed at wileyonlinelibrary.com]

regularization methods, respectively, and L*m* means the Landweber algorithm with *m* iterations. Note that, for each algorithm, CC and AAD are the average over the 78 randomly selected distributions. From Figure 6, it can be seen that the LBP and conventional Tikhonov methods give relatively low CC due to the poor quality of reconstructed images. With the Landweber iteration, as the number of iterations increases, CC rises quickly in the first 100 iterations and then shows a slow increase over the next 100 iterations. As the iteration process continues, a decrease in CC is noticed, demonstrating the semi-convergence characteristic of the Landweber iteration algorithm.[19] When the modified Tikhonov method is used, a value of 0.83, which is as high as that obtained by the Landweber algorithm with 25 iterations, can be reached. As for AAD, consistent with the results in Supporting Information Figure S5, Figure 6 also shows that a higher CC always corresponds to a lower AAD and vice versa.

To evaluate the stability of images reconstructed by different algorithms, error bars calculated from the standard deviations of CC and AAD over the 78 tested distributions are also shown in Figure 6 and a lower value of standard deviation implies the ability of an algorithm to produce images with consistent quality. The error bars indicate that the vibration of AAD for all algorithms is small, while the fluctuation of CC shows differences for different algorithms and, specifically, a remarkable fluctuation of CC occurs for the LBP, conventional Tikhonov regularization, and Landweber algorithm with iterations less than 15 and more than 300, while a less noticeable standard deviation holds for the modified Tikhonov and Landweber algorithm with iterations more than 15 and less than 300. It is therefore clear from Figure 6 that the modified Tikhonov method can improve not only the image quality but also the stability compared to the conventional Tikhonov method. Furthermore, the reconstruction stability obtained by the modified Tikhonov method is similar to that obtained by the Landweber algorithm with iterations more than 15 and less than 300. Therefore, it can be concluded from Figures 5 and 6 that both image quality and stability produced by the modified Tikhonov method are comparable to those produced by the Landweber method with 25 iterations.

Elapsed Time. One of the most attractive advantages of ECT is its high temporal resolution. With a twin-plane ECT sensor, flow velocity[47] and even velocity profile[48] in a

fluidized bed can be measured. For this purpose, both a rapid data acquisition hardware design and a high-speed algorithm are necessary. To compare the speed of different algorithms, the elapsed time in a reconstruction step required for different algorithms was evaluated on a PC with an Intel Core i5 3.30 GHz, as shown in Supporting Information Figure S6.

Because the matrix $(S^T S + \mu I)^{-1} S^T$ can be calculated and stored in advance,[20] both the conventional and modified Tikhonov regularization algorithms take the same computational time as the LBP method, which is approximately 0.3 ms. For the Landweber iteration, the computational time increases linearly with the number of iterations; more specifically, the time taken by the Landweber algorithm with 25 iterations and 200 iterations is approximately 30 and 230 ms, respectively, corresponding to roughly 100 and 800 times the elapsed time taken by the non-iterative algorithms, respectively.

Accuracy of the Overall Solid Concentration Measurement. Via pixel averaging, overall solid concentration can be measured. Figure 7a shows a histogram of the relative error associated with the measurement of the overall solid concentration using different image reconstruction algorithms in the 78 selected distributions. Note that the solid concentration in Figure 7a was calculated based on the most widely used parallel model,[44,45] as defined in Eq. 17. To test the effect of the used concentration model on the measurement of the overall
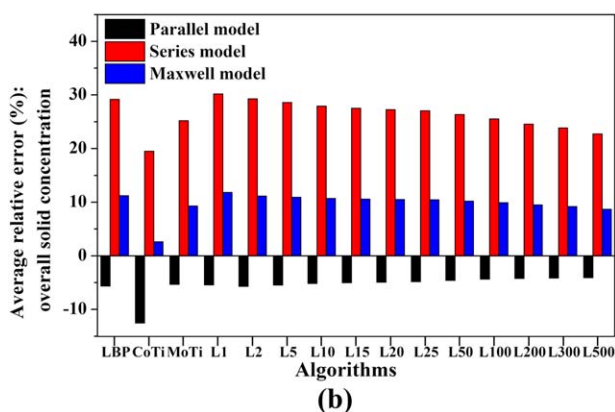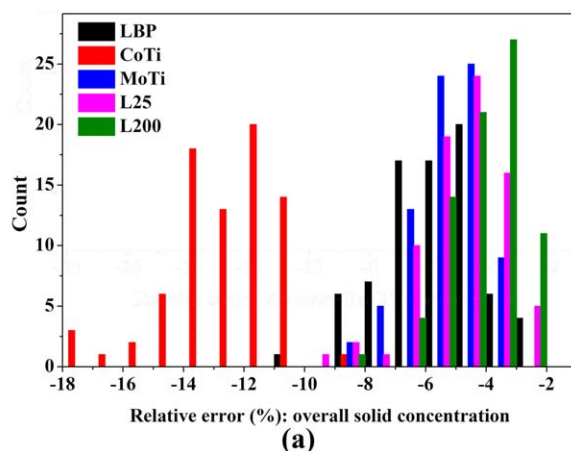

(a)

(b)

Figure 7. Evaluation of different image reconstruction algorithms for the overall solid concentration measurement: (a) histogram of the relative error and (b) effect of the concentration model on the average relative error over the 78 tested distributions.

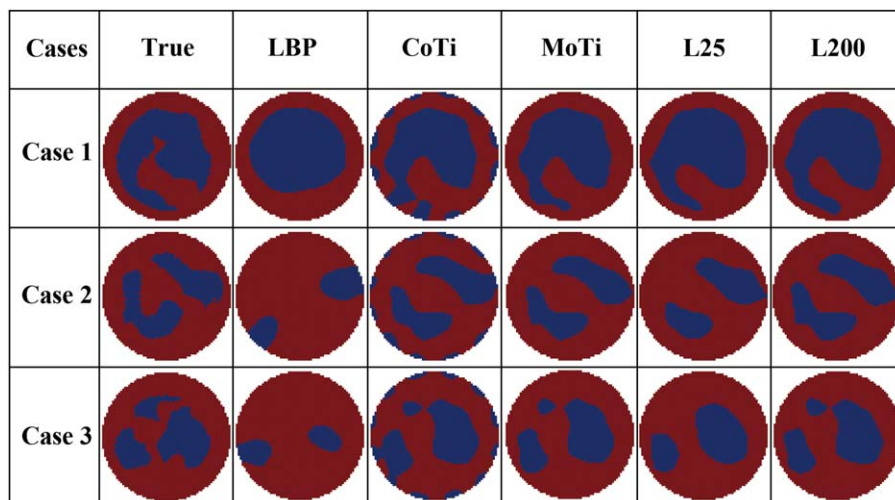[Color figure can be viewed at wileyonlinelibrary.com]

Figure 8. Cross-sectional bubble distributions reconstructed by different algorithms using CFD simulation results as the input permittivity distributions.

The red regions and blue regions represent emulsion and bubble phases, respectively. [Color figure can be viewed at wileyonlinelibrary.com]

solid concentration, Figure 7b shows the average relative error over the 78 selected distributions for the parallel model, series model, and Maxwell model.

As can be seen in Figure 7a, all algorithms underestimate the overall solid concentration in all cases and, except for the conventional Tikhonov regularization, all algorithms can give the overall concentration at the same level: the relative error is within −11% for all 78 cases and is approximately −5% on average (see Figure 7b). Figure 7 given by Wei et al.[20] also indicates a lower volume fraction reconstructed by the LBP, conventional Tikhonov regularization and Landweber iteration methods. A possible reason for the underestimation is that the transformation from permittivity distribution into material distribution uses the parallel model, in which the normalized permittivity and the normalized solid concentration take the same value. Some other concentration models, such as the series model and Maxwell model, set the value of the normalized solid concentration to be higher than the normalized permittivity.[16,44] In this way, the underestimation problem can be solved; however, a new overestimation problem emerges, as shown in Figure 7b. It is also noteworthy from Figure 7b that the average relative error obtained by the series model is much higher than that obtained by the Maxwell model, inferring that a new concentration model, which is in between the parallel model and Maxwell model, is highly desired.

Accuracy of the Bubble Size Measurement. In a fluidized bed, bubbles can affect fluidization quality, solid mixing, and inter-phase mass and heat transfer.[11,13,49] Therefore, accurate quantification of bubble size is important for the design and operation of a fluidized bed. However, in practice the definition of a bubble in gas–solid bubbling fluidized beds is ambiguous. As shown in Figure 5 and Supporting Information Animation S1, there is no a clear interface between bubble and emulsion phases and bubbles are surrounded by an extensive shell of solid particles in which the solid concentration increases gradually.[23] Therefore, to extract the bubble properties from the solid concentration distribution measured by ECT, a threshold is usually used to define the boundary between bubble and emulsion phases and this threshold ranges from 0.15 to 0.3 in literature.[11,50]

To evaluate different image reconstruction algorithms for their bubble detection accuracy, Figure 8 shows three typical bubble distributions extracted from the CFD simulation results and the corresponding images reconstructed by different algorithms, in which Case 1 represents a single-bubble distribution, Case 2 represents a two-bubble distribution, and Case 3 represents a three-bubble distribution. Note that the binary images in Figure 8 were obtained with a threshold solid concentration of 0.2. That is to say, the regions with the solid concentration lower than 0.2 were regarded as being in the bubble phase (the blue regions in Figure 8) and the other regions were classified as being in the emulsion phase (the red regions in Figure 8).

As is clear in Figure 8, the LBP method can only qualitatively reconstruct the single-bubble distribution in Case 1 and, for other two cases, the reconstructed bubble distributions show large deviations compared to the true images. For the conventional Tikhonov method, even though bubbles in the central area can be well reconstructed for all three cases, the unphysical artifacts make it difficult to interpret the reconstructed bubble distributions in a real application, because the artifacts will result in uncertainty as to whether there are bubbles near the wall. When the proposed modified Tikhonov method is used, the artifacts disappear and all the reconstructed bubble distributions are satisfied. In particular, the number of bubbles in all three cases is the same as that in the true images. As for the bubble shape, for the single-bubble distribution in Case 1, the modified Tikhonov method gives a similar result to the Landweber method with 25 iterations and, for multi-bubble distributions in Cases 2 and 3, the reconstructed bubble distributions are comparable to those by the Landweber method with 200 iterations.

To quantitatively evaluate different algorithms for the accuracy of bubble size measurement, Figure 9 compares equivalent bubble diameters calculated by different image reconstruction algorithms from the three cases shown in Figure 8. The equivalent bubble diameter was calculated following Verma et al.[51] First, the number of bubbles in an ECT image was detected using an edge detection method. Then, the area of each bubble was calculated as the surface area of the corresponding continuous region where the solid concentration
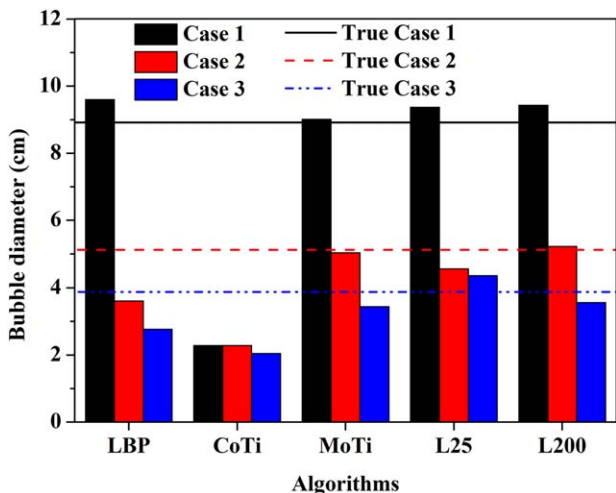
Figure 9. Evaluation of different image reconstruction algorithms for the bubble size measurement using CFD simulation results as the input permittivity distributions.

[Color figure can be viewed at wileyonlinelibrary.com]

is lower than 0.2. Next, the diameter of each bubble was obtained as the diameter of a circular bubble with equivalent cross-sectional area. Finally, the equivalent bubble diameter in the ECT image was obtained as the number-averaged bubble diameter. As the images reconstructed by the conventional Tikhonov method show many artifacts in the near-wall region, following the suggestions of Geldart[46] that a clearly recognizable bubble will have a diameter larger than 0.5 cm, some small bubbles with diameters smaller than 0.5 cm were excluded from the average.

As can be seen in Figure 9, because some artifacts in the near-wall region were included when calculating the equivalent bubble diameter, the conventional Tikhonov method underestimates the bubble size in all three cases. After the unphysical artifacts are removed by the modification, a high-accuracy estimation of the equivalent bubble diameter can be obtained: the relative errors for Cases 1 and 2 are 1.06% and −1.62%, respectively, and, for the three-bubble distribution in Case 3, the relative error also lies within −12%, say −11.3%. For the LBP method, it can only provide a satisfactory result for the single-bubble distribution in Case 1 with a relative error of 7.69%; for the other two cases, the relative errors are both beyond −25%. When the Landweber algorithm is used, for Case 1, both 25 and 200 iterations perform worse than the modified Tikhonov method; for Case 2, 200 iterations can provide a similar result to the modified Tikhonov method, while 25 iterations perform worse due to the poorly reconstructed bubble shapes; and for Case 3, 200 iterations give the closest estimation with a relative error of −7.73%, while 25 iterations overestimate the bubble size, because the smallest bubble in Case 3 cannot be reconstructed, as shown in Figure 8.

As the threshold solid concentration for the bubble definition ranges from 0.15 to 0.3 in literature,[11,50] the sensitivity of different algorithms to the choice of the threshold in bubble distribution reconstruction needs to be tested. Supporting Information Figure S7 shows a typical bubble distribution reconstructed by different algorithms using the thresholds of 0.15, 0.25, and 0.3; the corresponding bubble distribution using the threshold of 0.2 is shown in Figure 8 as Case 2. Clearly, the modified Tikhonov algorithm is robust for

quantitatively extracting bubble size and bubble shape in gas–solid bubbling fluidized beds and shows weak dependence on the choice of the threshold. It should be stressed, however, the choice of the threshold is a non-trivial task in real fluidized beds. A prior calibration[11,52] is necessary to obtain an optimal threshold and thus reasonable bubble distributions.

Accuracy of the Radial Solid Concentration Profile Measurement. Two representative distributions are shown in Figure 10a for a multi-bubble flow and in Figure 10b for a solid slug flow to compare the radial solid concentration profiles produced by different image reconstruction algorithms. Figure 10 shows that, except for the LBP method that shows a smoothing effect on the gradual transition between emulsion and bubble phases, all algorithms can quantitatively reconstruct the profile. However, for the conventional Tikhonov method, due to the artifacts shown in Figure 5, a large deviation near the wall is noted. While the curves produced by the modified Tikhonov method and Landweber method with 25 and 200 iterations nearly coincide with each other and approach the curve of the true profiles, showing the ability of
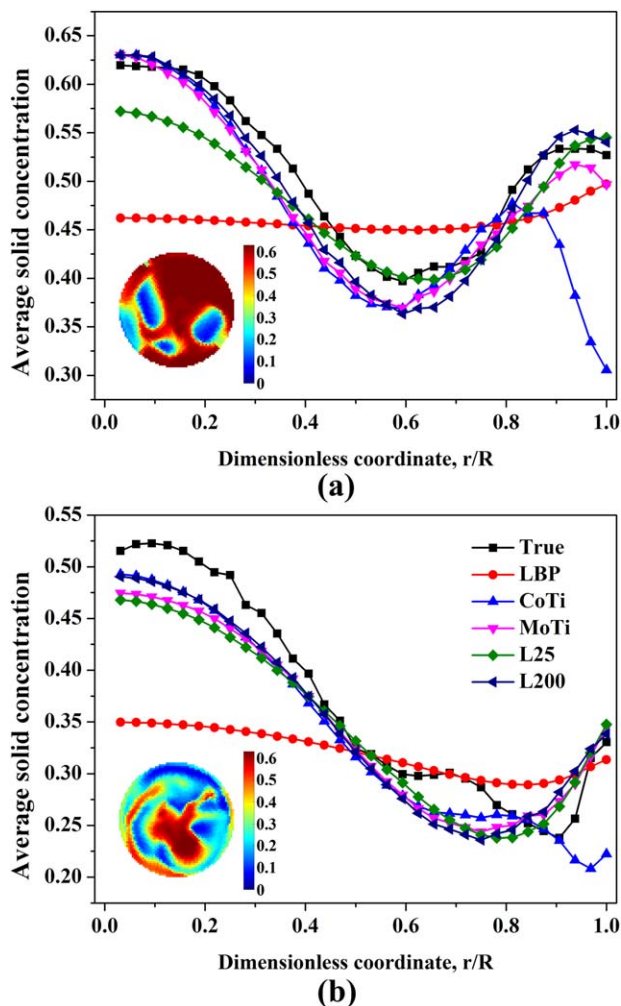

(a)

(b)

Figure 10. Accuracy of different image reconstruction algorithms with respect to the radial profile of solid concentration.

The inserted ECT images are true distributions from the CFD simulation results. The color scales represent the solid concentration. [Color figure can be viewed at wileyonlinelibrary.com]
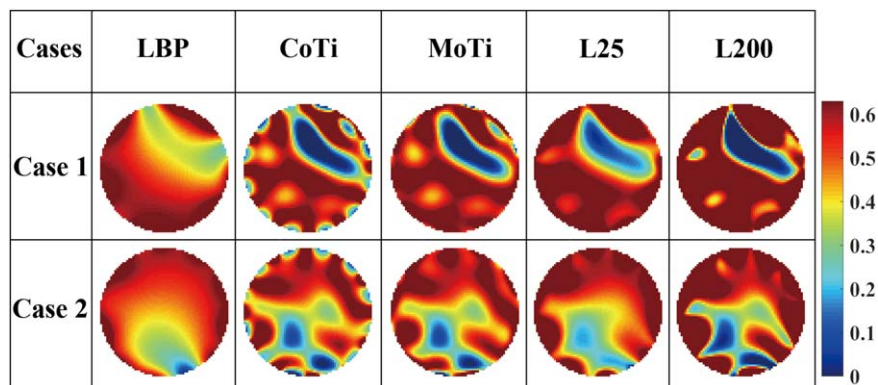
Figure 11. Cross-sectional solid concentration distributions reconstructed by different algorithms using experimental data.

The color scale represents the solid concentration. [Color figure can be viewed at wileyonlinelibrary.com]

these algorithms to provide the radial profile of solid concentration in an accurate manner.

Evaluation by experiments

To verify the feasibility of the modified Tikhonov regularization method for experiments, two key aspects obtained by different image reconstruction algorithms in experiments are discussed. They are image quality and equivalent bubble size.

Image Quality Comparison. Figure 11 shows two sets of typical images reconstructed by different algorithms using experimental data. The optimized regularization parameter from the numerical simulations, 0.0001, was used in experiments for both the conventional and modified Tikhonov methods. Even though the true distributions are unknown in a real fluidized bed, it is still clear from Figure 11 that there are artifacts in the near-wall region in the images reconstructed by the conventional Tikhonov method and that the distribution of the artifacts is the same as that in numerical simulations. With the modified Tikhonov method, the artifacts disappear and the images are as good as those of the Landweber method with 25 iterations (Case 1) or 200 iterations (Case 2). An additional comparison to the images reconstructed by the LBP method indicates that more details can be seen with the modified Tikhonov method without extensive computation.

Bubble Size Measurement. To quantify the bubble size determined by different image reconstruction algorithms in experiments, Figure 12 shows the equivalent bubble diameter calculated at each superficial gas velocity using the threshold solid concentration of 0.2 following previous works.[8,23,37] Because the studied fluidized bed had a small bed diameter of 6 cm and was operated with a large initial aspect ratio of 5.5, in most cases, it was observed that only a single bubble could pass through the ECT measurement region at a time. In addition, because the acquisition rate of the used AC-based ECT system was 100 Hz, each bubble could be detected several times when it passed through the measurement region. Therefore, the experimental equivalent bubble diameter was obtained as follows. First, the time series of ECT images at each superficial gas velocity was divided into 50 segments, with each segment corresponding to a time duration of 2 s. Then, the maximum equivalent bubble diameter in each segment was detected. Finally, the average of the 50 maximum equivalent bubble diameters was chosen to represent the characteristic bubble size at a given superficial gas velocity. The

error bars in Figure 12 were calculated as the standard deviation of the 50 maximum equivalent bubble diameters.

To compare the measured bubble size with the established empirical correlations, the estimated bubble diameters from the correlations of Darton et al.[49] and Werther[53] are shown alongside the experimental size in Figure 12. Note that the correlations of Darton et al.[49] and Werther[53] were originally developed in beds with the diameter larger than 10 cm; therefore, these two correlations can only play a qualitative rather than a quantitative role when evaluating the bubble size reconstructed by different algorithms using experimental data.

As shown in Figure 12, the equivalent bubble diameter calculated using different algorithms and the two correlations have a similar tendency, showing an increase in bubble size with the increase in superficial gas velocity. Excepting that the equivalent diameters calculated by the conventional Tikhonov method are much smaller than those of the two correlations, the diameters calculated by the other techniques lie within the window of the two correlations, especially when the superficial gas velocity is larger than approximately five times the
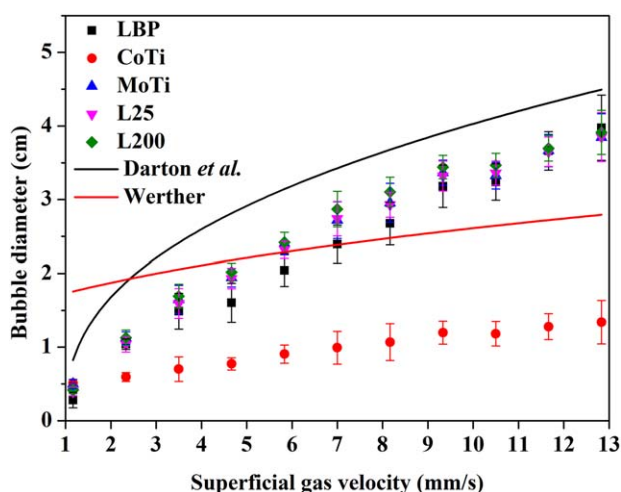

Figure 12. Bubble size determined by different image reconstruction algorithms in experiments and the correlations of Darton et al.[49] and Werther.[53]

The error bars are calculated as the standard deviation of the 50 maximum equivalent bubble diameters. [Color figure can be viewed at wileyonlinelibrary.com]

minimum bubbling velocity. Comparing Figure 12 to Figure 9, it can be seen that the experimental data is in good agreement with the simulations. In both situations, the conventional Tikhonov method gives the smallest measurements of the equivalent bubble diameter due to the artifacts in the near-wall region, while the bubble diameters calculated by the modified Tikhonov method fall in between those calculated by the Landweber method with 25 and 200 iterations.

Conclusion

In this work, a similar one-to-one division operation, which was originally used in the LBP method, is introduced to modify the conventional Tikhonov method for the use of ECT in gas–solid bubbling fluidized bed measurements. Both numerical simulations and experiments were performed to evaluate the proposed algorithm. In particular, the simulations were performed by comparing the reconstructed images with the cross-sectional solid concentration distributions extracted from CFD simulation results. In addition to the image quality, the accuracy of the modified Tikhonov method when obtaining some key hydrodynamic characteristics in gas–solid bubbling fluidized beds, such as the overall solid concentration, bubble size, and radial solid concentration profile, was systemically evaluated. Based on this work, the conclusions can be summarized as follows:

● The LBP, Tikhonov regularization, and Landweber iteration methods are three most popular algorithms for ECT. The LBP and Tikhonov regularization methods are good for on-line measurements due to their fast speed. However, images reconstructed by the LBP method are usually blurred. With the conventional Tikhonov method, even though basically satisfactory results can be obtained in the central area, artifacts always occur in the near-wall region and the problem of artifacts is more severe in the case of low-permittivity materials presenting in a high-permittivity background, which is exactly the case in a gas–solid bubbling fluidized bed, where discrete bubbles are dispersed in a continuous emulsion phase. As for the Landweber iteration algorithm, the best images in most cases can be produced; however, its computational cost prevents it from on-line applications.

● The main reason for the artifacts shown in images reconstructed by the conventional Tikhonov method is the non-uniform distribution of the sensitivity in the generic sensitivity matrix. The division operation introduced to modify the conventional Tikhonov method can rescale the gray level in each pixel, and therefore the artifacts can be effectively removed.

● The regularization parameter in both the conventional and modified Tikhonov methods can be determined by obtaining the highest value of CC and the lowest value of AAD.

● The quality of images reconstructed by the modified Tikhonov method is comparable to that reconstructed by the Landweber iteration method with dozens of iterations, while the computational cost of the modified Tikhonov method is only one percent or less of that of the Landweber iteration.

● The modified Tikhonov method shows high accuracy or the same accuracy as the Landweber iteration algorithm when obtaining the overall solid concentration, bubble size, and profile of radial solid concentration in gas–solid bubbling fluidized beds. Therefore, the modified Tikhonov method has the potential to become an efficient on-line image reconstruction method for ECT measurements of gas–solid bubbling fluidized beds.

● The overall solid concentration is underestimated by the parallel model for all test algorithms in this article. If the concentration model is changed to the series or Maxwell models, a new overestimation problem emerges. Furthermore, the relative error obtained by the series model is much higher than that obtained by the Maxwell model. This suggests that a new concentration model, which is in between the parallel model and Maxwell model, is needed.

● It is reasonable to speculate that the proposed modified Tikhonov method can also be applied to ECT measurements of bubble columns with high accuracy, because bubble columns are similar to gas–solid bubbling fluidized beds in terms of a low-permittivity bubble phase dispersing in a high-permittivity background.

Notation

Roman letters

C = capacitance, pF
V = potential difference, V
S = normalized sensitivity matrix
N = the number of pixels in an ECT image
I = identity matrix (ones on the main diagonal and zeros elsewhere)
e = capacitance residual
g = normalized permittivity

Greek letters

ε_r = relative permittivity
φ = potential distribution, V
λ = normalized capacitance
u_λ = identity vector (a vector of ones)
μ = regularization parameter
α = step length
ϕ = concentration
Δ = characteristic grid width, mm
δ = Gaussian distributed random noise

Subscripts

g = air phase
s = solid phase
L = low calibration
H = high calibration
M = measurement

Superscript

$-$ = average value
$\hat{}$ = reconstructed value

Abbreviations

ECT = electrical capacitance tomography
LBP = linear back projection
CFD = computational fluid dynamics
CC = correlation coefficient
AAD = average absolute deviation
FCC = fluid catalytic cracking
SNR = signal-to-noise ratio, dB

Literature Cited

1. Almstedt AE, Zakkay V. An investigation of fluidized-bed scaling capacitance probe measurements in a pressurized fluidized-bed combustor and a cold model bed. *Chem Eng Sci.* 1990;45:1071–1078.

2. Werther J. Measurement techniques in fluidized beds. *Powder Technol*. 1999;102:15–36.

3. Yao JF, Takei M. Application of process tomography to multiphase flow measurement in industrial and biomedical fields: a review. *IEEE Sens J*. 2017; in press.

4. Johnsson F, Zijerveld RC, Schouten JC, van den Bleek CM, Leckner B. Characterization of fluidization regimes by time-series analysis of pressure fluctuations. *Int J Multiphase Flow*. 2000;26:663–715.

5. Johnsson H, Johnsson F. Measurements of local solids volume-fraction in fluidized bed boilers. *Powder Technol*. 2001;115:13–26.

6. Makkawi YT, Wright PC. Fluidization regimes in a conventional fluidized bed characterized by means of electrical capacitance tomography. *Chem Eng Sci*. 2002;57:2411–2437.

7. Yang WQ. Design of electrical capacitance tomography sensors. *Meas Sci Technol*. 2010;21:042001.

8. McKeen T, Pugsley T. Simulation and experimental validation of a freely bubbling bed of FCC catalyst. *Powder Technol*. 2003;129:139–152.

9. Zhang WB, Wang C, Yang WQ, Wang C-H. Application of electrical capacitance tomography in particulate process measurement: a review. *Adv Powder Technol*. 2014;25:174–188.

10. van Buijtenen MS, Buist K, Deen NG, Kuipers JAM, Leadbeater T, Parker DJ. Numerical and experimental study on spout elevation in spout-fluidized beds. *AlChE J*. 2012;58:2524–2535.

11. Weber JM, Mei JS. Bubbling fluidized bed characterization using Electrical Capacitance Volume Tomography (ECVT). *Powder Technol*. 2013;242:40–50.

12. Zhang WB, Cheng YP, Wang C, Yang WQ, Wang C-H. Investigation on hydrodynamics of triple-bed combined circulating fluidized bed using electrostatic sensor and electrical capacitance tomography. *Ind Eng Chem Res*. 2013;52:11198–11207.

13. Chandrasekera TC, Li Y, Moody D, Schnellmann MA, Dennis JS, Holland DJ. Measurement of bubble sizes in fluidised beds using electrical capacitance tomography. *Chem Eng Sci*. 2015;126:679–687.

14. Xie CG, Huang SM, Hoyle BS, Thorn R, Lenn C, Snowden D, Beck MS. Electrical capacitance tomography for flow imaging: system model for development of image-reconstruction algorithms and design of primary sensors. *IEE Proc G Circuits Dev Syst*. 1992;139:89–98.

15. Yang WQ, Peng LH. Image reconstruction algorithms for electrical capacitance tomography. *Meas Sci Technol*. 2003;14:R1–R13.

16. Banaei M, van Sint Annaland M, Kuipers JAM, Deen NG. On the accuracy of Landweber and Tikhonov reconstruction techniques in gas–solid fluidized bed applications. *AlChE J*. 2015;61:4102–4113.

17. Cui ZQ, Wang Q, Xue Q, Fan WR, Zhang LL, Cao Z, Sun BY, Wang HX, Yang WQ. A review on image reconstruction algorithms for electrical capacitance/resistance tomography. *Sens Rev*. 2016;36:429–445.

18. Yang WQ, York TA. New AC-based capacitance tomography system. *IEE Proc Sci Meas Technol*. 1999;146:47–53.

19. Lei J, Liu S, Li ZH, Sun M. An image reconstruction algorithm based on the extended Tikhonov regularization method for electrical capacitance tomography. *Measurement*. 2009;42:368–376.

20. Wei K, Qiu CH, Soleimani M, Primrose K. ITS reconstruction toolsuite: an inverse algorithm package for industrial process tomography. *Flow Meas Instrum*. 2015;46:292–302.

21. Peng LH, Merkus H, Scarlett B. Using regularization methods for image reconstruction of electrical capacitance tomography. *Part Part Syst Charact*. 2000;17:96–104.

22. Xue Q, Wang HX, Cui ZQ, Yang CY. Electrical capacitance tomography using an accelerated proximal gradient algorithm. *Rev Sci Instrum*. 2012;83:043704.

23. Yates JG, Cheesman DJ, Sergeev YA. Experimental observations of voidage distribution around bubbles in a fluidized bed. *Chem Eng Sci*. 1994;49:1885–1895.

24. Pugsley T, Tanfara H, Malcus S, Cui H, Chaouki J, Winters C. Verification of fluidized bed electrical capacitance tomography measurements with a fibre optic probe. *Chem Eng Sci*. 2003;58:3923–3934.

25. Tikhonov AN, Arsenin VY. *Solutions of Ill-Posed Problems*. Washington, DC: Vh Winston, 1977.

26. Zhao JC, Fu WL, Li TS, Wang S. An image reconstruction algorithm based on a revised regularization method for electrical capacitance tomography. *Meas Sci Technol*. 2002;13:638–640.

27. Li Y, Yang WQ. Image reconstruction by nonlinear Landweber iteration for complicated distributions. *Meas Sci Technol*. 2008;19:094014

28. Hochstenbach ME, Reichel L. Fractional Tikhonov regularization for linear discrete ill-posed problems. *BIT Numer Math*. 2011;51:197–215.

29. Sun XS, Liu J, Han X, Jiang C, Chen R. A new improved regularization method for dynamic load identification. *Inverse Probl Sci Eng*. 2013;22:1062–1076.

30. Hochstenbach ME, Reichel L, Rodriguez G. Regularization parameter determination for discrete ill-posed problems. *J Comput Appl Math*. 2015;273:132–149.

31. Bazán FSV. Simple and efficient determination of the Tikhonov regularization parameter chosen by the generalized discrepancy principle for discrete ill-posed problems. *J Sci Comput*. 2014;63:163–184.

32. Peng LH, Ye JM, Lu G, Yang WQ. Evaluation of effect of number of electrodes in ECT sensors on image quality. *IEEE Sensor J*. 2012;12:1554–1565.

33. Rabha S, Schubert M, Wagner M, Lucas D, Hampel U. Bubble size and radial gas hold-up distributions in a slurry bubble column using ultrafast electron beam X-ray tomography. *AlChE J*. 2013;59:1709–1722.

34. Singh BK, Quiyoom A, Buwa VV. Dynamics of gas–liquid flow in a cylindrical bubble column: comparison of electrical resistance tomography and voidage probe measurements. *Chem Eng Sci*. 2017;158:124–139.

35. Ye JM, Wang HG, Yang WQ. Evaluation of electrical capacitance tomography sensor based on the coupling of fluid field and electrostatic field. *Meas Sci Technol*. 2016;27:074003.

36. Yang WQ, Liu S. Role of tomography in gas/solids flow measurement. *Flow Meas Instrum*. 2000;11:237–244.

37. Zhang JL, Mao MX, Ye JM, Wang HG, Yang WQ. Investigation of wetting and drying process in a gas–solid fluidized bed by electrical capacitance tomography and pressure measurement. *Powder Technol*. 2016;301:1148–1158.

38. Yang WQ, Spink DM, York TA, McCann H. An image-reconstruction algorithm based on Landweber's iteration method for electrical-capacitance tomography. *Meas Sci Technol*. 1999;10:1065–1069.

39. Liu S, Fu L, Yang WQ. Optimization of an iterative image reconstruction algorithm for electrical capacitance tomography. *Meas Sci Technol*. 1999;10:L37–L39.

40. Ye JM, Wang HG, Li Y, Yang WQ. Coupling of fluid field and electrostatic field for electrical capacitance tomography. *IEEE Trans Instrum Meas*. 2015;64:3334–3353.

41. Sinclair JL, Jackson R. Gas-particle flow in a vertical pipe with particle-particle interactions. *AlChE J*. 1989;35:1473–1486.

42. Li Y, Holland DJ. Fast and robust 3D electrical capacitance tomography. *Meas Sci Technol*. 2013;24:105406.

43. Rasel RK, Zuccarelli CE, Marashdeh QM, Fan L-S, Teixeira FL. Towards multiphase flow decomposition based on electrical capacitance tomography sensors. *IEEE Sens J*. 2017; in press.

44. Yang WQ, Chondronasios A, Nattrass S, Nguyen VT, Betting M, Ismail I, McCann H. Adaptive calibration of a capacitance tomography system for imaging water droplet distribution. *Flow Meas Instrum*. 2004;15:249–258.

45. Du B, Warsito W, Fan L-S. ECT studies of the choking phenomenon in a gas–solid circulating fluidized bed. *AlChE J*. 2004;50:1386–1406.

46. Geldart D. Types of gas fluidization. *Powder Technol*. 1973;7:285–292.

47. Rao SM, Zhu KW, Wang C-H, Sundaresan S. Electrical capacitance tomography measurements on the pneumatic conveying of solids. *Ind Eng Chem Res*. 2001;40:4216–4226.

48. Dashliborun AM, Larachi F, Hamidipour M. Cyclic operation strategies in inclined and moving packed beds-potential marine applications for floating systems. *AlChE J*. 2016;62:4157–4172.

49. Darton RC, Lanauze RD, Davidson JF, Harrison D. Bubble growth due to coalescence in fluidized beds. *Trans Inst Chem Eng*. 1977;55:274–280.

50. Sobrino C, Acosta-Iborra A, Izquierdo-Barrientos MA, de Vega M. Three-dimensional two-fluid modeling of a cylindrical fluidized bed and validation of the maximum entropy method to determine bubble properties. *Chem Eng J*. 2015;262:628–639.

51. Verma V, Padding JT, Deen NG, Kuipers JAM, Barthel F, Bieberle M, Wagner M, Hampel U. Bubble dynamics in a 3-D gas–solid fluidized bed using ultrafast electron beam X-ray tomography and two-fluid model. *AlChE J*. 2014;60:1632–1644.

52. Rautenbach C, Melaaen MC, Halvorsen BM. Statistical diagnosis of a gas–solid fluidized bed using electrical capacitance tomography. *Int J Multiphase Flow*. 2013;49:70–77.

53. Werther J. Effect of gas distributor on the hydrodynamics of gas fluidized beds. *Ger Chem Eng*. 1978;1:166–174.